PHYSICAL REVIEW D VOLUME 47, NUMBER 1 1 JANUARY 1993

ARTICLES

Study of electron-neutrino–electron elastic scattering at LAMPF

R. C. Allen,[a] H. H. Chen,[b] P. J. Doe,[c] R. Hausammann,[d] W. P. Lee,[e]
X. Q. Lu,[f] H. J. Mahler,[g] M. E. Potter,[c] and K. C. Wang[h]
University of California, Irvine, California 92717

T. J. Bowles, R. L. Burman, R. D. Carlini,[i] D. R. F. Cochran, J. S. Frank,[j]
E. Piasetzky,[k] and V. D. Sandberg
Los Alamos National Laboratory, Los Alamos, New Mexico 87545

D. A. Krakauer and R. L. Talaga
Argonne National Laboratory, Argonne, Illinois 60439
and University of Maryland, College Park, Maryland 20742
(Received 17 June 1992)

Neutrino-electron elastic scattering was observed with a 15-ton fine-grained tracking calorimeter exposed to electron neutrinos from muon decay at rest. The measured $\nu_e e^- \rightarrow \nu_e e^-$ elastic scattering rate of 236 ± 35 events yields the total elastic scattering cross section $10.0 \pm 1.5(\text{stat}) \pm 0.9(\text{syst}) \times 10^{-45}$ cm$^2 \times [E_\nu$ (MeV)], and a model-independent measurement of the strength of the destructive interference between the charged and neutral currents, $I = -1.07 \pm 0.21$, that agrees well with the standard model (SM) prediction $I = -1.08$. The agreement between the measured electroweak parameters and SM expectations is used to place limits on neutrino properties, such as neutrino flavor-changing neutral currents and neutrino electromagnetic moments. Limits are placed on the masses of new bosons that interact with leptons: for a neutral tensor boson, $M_T > 105$ GeV; for a neutral (pseudo)scalar boson, $M_{P,S} > 47$ GeV; for a charged Higgs boson, $M_{\chi^+} > 87$ GeV; and for a purely left-handed charged (neutral) vector boson, $M_x > 239$ (119) GeV.

PACS number(s): 13.10.+q, 12.15.Mm, 14.60.Gh, 14.80.−j

I. INTRODUCTION

Neutrino-electron scattering is a simple and fundamental process with great sensitivity to aspects of the standard model, including dynamic properties of the weak interaction, such as the weak mixing angle $\sin^2\theta_W$ and the interference between charged- and neutral-current amplitudes, and static properties of the neutrino, such as electromagnetic moments. It is a purely weak, purely leptonic two-body reaction which makes both the theoretical cross-section calculations and the experimental signatures straightforward. This report describes the final results of the first experiment [1] to observe the elastic scattering reaction $\nu_e e^- \rightarrow \nu_e e^-$. Measurement of the absolute cross section for this reaction provides the definitive test of the interference between $W^\pm$- and Z^0-boson exchange.

The experimental signature for the two-body elastic reaction $\nu e^- \rightarrow \nu e^-$ was exceedingly simple: the signal was a single, minimum-ionizing particle track appearing at small angles relative to the incident neutrino direction. From a clear observation of 295 νe^- events, this experiment obtained the first measurement of the interference between the weak charged- and neutral-current amplitudes [2]. The model-independent measurement of the $\nu_e e^-$ cross section was also interpreted in terms of a measurement of the weak neutral-current parameter $\sin^2\theta_W$ and as limits against nonstandard electroweak couplings. The good agreement of these measurements with predictions of the standard model allowed very stringent limits on electromagnetic interactions of neutrinos (both electron and muon type), and on the existence of new gauge bosons.

The elastic scattering of electron neutrinos by electrons, $\nu_e e^- \rightarrow \nu_e e^-$, occurs through the exchange of both $W^\pm$ and Z^0 bosons as shown by the Feynman dia-

[a] Now at Hewlett-Packard, Palo Alto, CA 94304.
[b] Deceased.
[c] Now at Los Alamos National Laboratory, Los Alamos, NM 87545.
[d] Now at Keller AG, Winterthur, Switzerland.
[e] Now at Jet Propulsion Laboratory, Pasadena, CA 91109.
[f] Now at Harvard Medical School, Boston, MA 02115.
[g] Now at Cerebus AG, Mannedorf, Switzerland.
[h] Now at Rockwell International, Thousand Oaks, CA 91350.
[i] Now at Continuous Electron Beam Accelerator Facility, Newport News, VA 23606.
[j] Now at Brookhaven National Laboratory, Upton, NY 11973.
[k] Permanent address: Tel-Aviv University, Ramat Aviv, Israel 69978.

grams in Fig. 1. Therefore, the cross section is sensitive to the interference (I) of the weak neutral-current (NC) and weak charged-current (CC) amplitudes [3, 4]. Although precise measurements of $\sin^2\theta_W$ now probe some aspects of the standard model (SM) at the level of radiative corrections [5], the NC/CC interference present in $\nu_e e^- \rightarrow \nu_e e^-$ represents a tree-level prediction that had not been confronted before the present experiment.

In the SM electroweak theory, the NC/CC interference term I is fixed by the value of $\sin^2\theta_W$. For $\sin^2\theta_W = 0.23$, the interference is destructive and reduces the elastic scattering cross section by 40% relative to a purely charged-current interaction. The interference strength as a function of $\sin^2\theta_W$ is an absolute prediction of the SM, and cannot be adjusted by modification of other parameters. This experiment measured the $\nu_e e^- \rightarrow \nu_e e^-$ elastic scattering cross section with sufficient precision to unambiguously demonstrate the destructive nature of the NC/CC interference [2]. The magnitude of I was found to be in excellent agreement with the accepted SM value.

Beyond its importance as a test of the SM, measurement of (any) nonzero value for I has several fundamental ramifications, some of which cannot be experimentally confirmed by other means. For instance, observation of interference between the NC and CC amplitudes shows that the final-state leptons are identical for both interactions. As the flavor and $V-A$ space-time structure of the CC is now well established, interference with the NC directly confirms the (V,A) nature of the neutral current and verifies that the outgoing neutrino from the CC is not an orthogonal flavor to the NC neutrino. Quantitative limits on non-(V,A) components of the NC and limits on neutrino flavor-changing currents are derived from the interference strength measurement reported here.

In principle, the NC/CC interference could be studied in several other processes accessible to laboratory experiments. Figure 2 illustrates Feynman diagrams for reactions where some experimental results have been reported. The earliest experimental results [6] had come from electron-antineutrino–electron elastic scattering [Fig. 2(a)] using reactor antineutrinos. The measured $\overline{\nu}_e e^- \rightarrow \overline{\nu}_e e^-$ cross section [6] is in agreement with the expected destructive interference, but is also consistent with a purely charged-current interaction. The experimental errors are therefore too large to make a quantitative statement on the weak interference.

The "single-photon production" reaction, $e^+e^- \rightarrow \gamma\nu\overline{\nu}$ [Fig. 2(b)], is sensitive to the NC/CC interference through the $\gamma\nu_e\overline{\nu}_e$ final state. The OPAL group has measured this reaction at the Z^0 pole, where the NC/CC interference term is expected to produce a 10% correction to the cross section determined from Z exchange only. Approximately 70 $e^+e^- \rightarrow \gamma\nu\overline{\nu}$ events were observed [7]. The results are in agreement with the SM, but no statement on the NC/CC interference has been made.

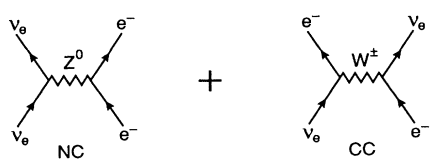

FIG. 1. Feynman diagram for $\nu_e + e^- \rightarrow \nu_e + e^-$ showing the weak charged- and neutral-current amplitudes.

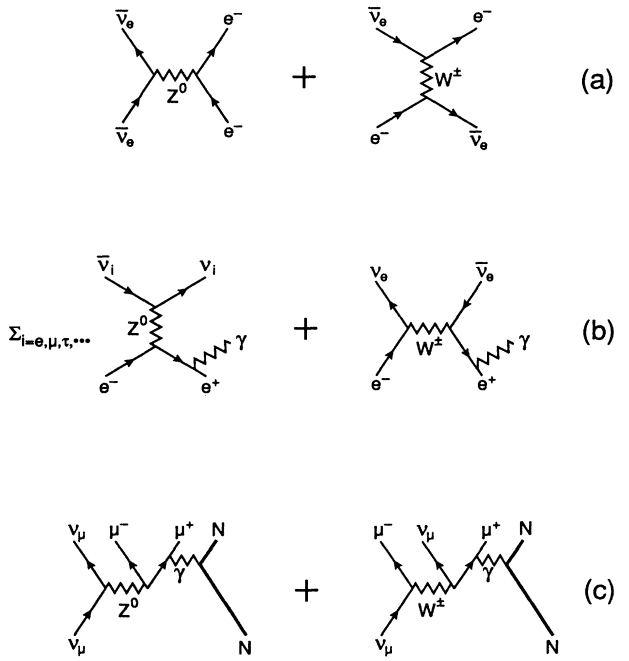

FIG. 2. Feynman diagrams for reactions sensitive to the interference between the weak charged- and neutral-current amplitudes: (a) $\overline{\nu}_e + e^- \rightarrow \overline{\nu}_e + e^-$, (b) $e^+ + e^- \rightarrow \overline{\nu} + \nu + \gamma$, and (c) $\nu_\mu + N \rightarrow \nu_\mu + \mu^- + \mu^+ + N$.

Progress has been made towards a measurement of interference in the coherent trilepton reaction, $\nu_\mu + N \rightarrow \nu_\mu + \mu^+ + \mu^- + N$ [Fig. 2(c)]. Low statistics, coupled with the intrinsic difficulty of calculating the electromagnetic initial state, has limited the significance of these results with respect to the weak interference. The CHARM-II group has reported 55 ± 17 events, in comparison with the SM expected rate of 35 [8]. More recently, the Chicago-Columbia-Fermilab-Rochester experiment observed [9] 15.6 ± 5.3 events, in agreement with the SM, and almost 2.5 σ below the expectation for a purely CC interaction.

A. Theoretical formalism

This section describes in detail the NC/CC interference term and how it can be measured in a model-independent manner in $\nu_e e^-$ elastic scattering using only experimental quantities. The purely neutral current portion of the Lagrangian for νe^- scattering is

$$\mathcal{L}^{\mathrm{NC}} = -\frac{G_F}{\sqrt{2}}\left(\overline{\nu_e}\gamma_\mu\frac{1-\gamma_5}{2}\nu_e\right) \times\left(\overline{e}\gamma^\mu\left[g_L\frac{1-\gamma_5}{2}+g_R\frac{1+\gamma_5}{2}\right]e\right), \quad (1)$$

where g_L and g_R are the electron chiral coupling constants to the weak neutral current. The Lagrangian (1) leads to the differential cross section

$$\frac{d\sigma}{dy} = \frac{m_e G_F^2 E_\nu}{2\pi}\left(g_L^2 + g_R^2(1-y)^2 + g_L g_R \frac{m_e y}{E_\nu}\right) , \quad (2)$$

where y is the energy fraction transferred from the incident neutrino to the recoil electron, $y = E_e/E_\nu$. Integration of $d\sigma/dy$, neglecting the term proportional to m_e/E_ν, yields the total cross section

$$\sigma^{\rm NC} = \frac{m_e G_F^2 E_\nu}{2\pi}\left(g_L^2 + \frac{1}{3}g_R^2\right) = \sigma_0\left(g_L^2 + \frac{1}{3}g_R^2\right) . \quad (3)$$

The cross section is proportional to the incident neutrino energy, and the proportionality constant σ_0/E_ν ($\sigma_0 = G_F^2 s/4\pi$) has the numerical value of 4.30×10^{-45} cm^2/MeV. For this measurement the average neutrino energy is $\langle E_{\nu_e}\rangle = 31.7$ MeV, so $\sigma_0 = 1.36 \times 10^{-43}$ cm^2.

Note that the cross section, Eq. (2), with the neglect of the last term, can be expressed as the sum of two incoherent components: the first due to scattering by electrons with the same ("left-handed") helicity as the neutrino, and the other due to scattering by electrons with the opposite ("right-handed") helicity. In the center of mass, the first term has a uniform distribution, whereas the second term has a $(1-\cos\theta)^2$ differential distribution.

The purely charged current portion of the $\nu_e e^-$ scattering Lagrangian is, after Fierz reordering,

$$\mathcal{L}^{\rm CC} = -\sqrt{2}G_F\left(\overline{\nu_e}\gamma_\mu\frac{1-\gamma_5}{2}\nu_e\right)\left(\overline{e}\gamma^\mu\frac{1-\gamma_5}{2}e\right) . \quad (4)$$

As an ansatz to maintain similarity to the neutral current cross section, one can define charged current "chiral couplings" $C_{L,R}$ by inspection of Eq. (4): $C_L = 2$, $C_R = 0$. These values reflect the well-established fact that the weak charged current is purely left handed. The charged current contribution to the $\nu_e e$ elastic scattering total cross section is simply

$$\sigma^{\rm CC} = C_L^2\sigma_0 = 4\sigma_0 . \quad (5)$$

The charged current and neutral current amplitudes are combined to obtain the full $\nu_e e^-$ scattering Lagrangian, $\mathcal{L}^{\nu_e e} = \mathcal{L}^{\rm CC} + \mathcal{L}^{\rm NC}$, by adding (4) to (1):

$$\mathcal{L}^{\nu_e e} = -\frac{G_F}{\sqrt{2}}\left(\overline{\nu_e}\gamma_\mu\frac{1-\gamma_5}{2}\nu_e\right) \times\left(\overline{e}\gamma^\mu\left[(C_L+g_L)\frac{1-\gamma_5}{2} +(C_R+g_R)\frac{1+\gamma_5}{2}\right]e\right). \quad (6)$$

The total cross section for electron-neutrino–electron elastic scattering is immediately obtained:

$$\sigma^{\rm tot} = (C_L^2 + 2C_L g_L + g_L^2 + \tfrac{1}{3}g_R^2)\sigma_0 = \sigma^{\rm CC} + \sigma^I + \sigma^{\rm NC}. \quad (7)$$

The term corresponding to the NC/CC interference, σ^I, has been explicitly separated from the previously defined charged- and neutral-current contributions, $\sigma^I = 2C_L g_L \sigma_0$. In order to conform to conventional expressions for an interference term, we introduce a coefficient I that measures the interference strength, $\sigma^I = 2I\sigma_0$, or

$$I = \sigma^I/2\sigma_0. \quad (8)$$

Note that we can regroup the neutral-current chiral couplings into vector and axial-vector couplings: $g_V = \frac{1}{2}(g_L + g_R)$ and $g_A = \frac{1}{2}(g_L - g_R)$. Within the SM, these couplings are given in terms of the single mixing parameter $\sin^2\theta_W$, as $g_V = -1/2 + 2\sin^2\theta_W$ and $g_A = -1/2$.

B. Measurement of the NC/CC interference strength

The interference term is measured directly, and in a model-independent manner, by the difference between the measured elastic scattering total cross section and the sum of the two "conventional" contributions:

$$\sigma^I = \sigma^{\rm tot} - \sigma^{\rm CC} - \sigma^{\rm NC} . \quad (9)$$

The conventional terms $\sigma^{\rm CC}$ and $\sigma^{\rm NC}$ have been measured to high precision in purely leptonic charged-current and neutral-current processes. The charged-current contribution $\sigma^{\rm CC}$ is taken to be exactly $4\sigma_0$, with the value σ_0 fixed by G_F as measured in muon decay [10]. The neutral-current contribution $\sigma^{\rm NC}$ can be obtained from absolute cross sections for muon-neutrino electron scattering; it is exactly equal to the cross section for $\nu_\mu e^- \to \nu_\mu e^-$ scattering at equal neutrino energy. Absolute measurement [11,12] of the total muon-neutrino–electron elastic scattering cross section is $\sigma^{\rm NC} = 0.442 \pm 0.065\ \sigma_0$.

With these inputs from purely leptonic reactions, and the assumption of e-μ universality, σ^I can be measured in a model-independent manner using only experimental values. Comparisons of the measured interference strength with theoretical predictions can be used to determine numerical limits on processes outside of the minimal SM theory. In the SM, where $C_L = 2$, $g_L = -1 + 2\sin^2\theta_W$, $\sigma^I = (-4 + 8\sin^2\theta_W)\sigma_0$. For $\sin^2\theta_W = 0.23$, the SM predicts $I = -2 + 4\sin^2\theta_W = -1.08$.

C. Tests relying on measurements of the interference

The intriguing possibility that the neutral current does not conserve neutrino flavor can be tested directly by the measurement of the NC/CC interference [13]. A neutrino flavor-changing neutral current (FCNC) would not be manifest in other laboratory NC experiments where the flavor of the outgoing neutrino is simply not observed. However, in this experiment, the flavor of the NC neutrino is tested by its ability to interfere with the (electron-flavor) neutrino emerging from the CC interaction. This experiment can determine upper limits on the magnitude of possible neutrino FCNC's from the difference between

the SM prediction and the measured NC/CC interference term.

A change in the magnitude of the interference effect in $\nu_e e^-$ scattering would be expected for the exchange of particles with spin differing from one, or for the presence of additional spin-1 bosons. For example, the exchange of a scalar Higgs boson, or of any new scalar (S), pseudoscalar (P), or tensor (T) bosons could introduce anomalous contributions to the total cross section with an (S, P, T) space-time structure. Limits on the strength of (S, P, T) interactions can be obtained from the observed cross section by noting that such interactions would lead to anomalous interaction rates.

D. Electromagnetic properties of the electron neutrino

The electroweak parameter $\sin^2\theta_W$ has been measured to high precision using various experimental techniques. The expected neutrino-electron scattering cross section can be predicted from these previous measurements of $\sin^2\theta_W$ using Eq. (7) with the SM values for g_L and g_R. If the neutrino also interacts electromagnetically, the observed neutrino-electron scattering rate will be altered from the SM rate. Therefore, the agreement of the observed rate with the theoretically expected rate can be used to place experimental limits on the intrinsic electromagnetic properties of the neutrino.

For example, a neutrino magnetic moment would introduce an incoherent increase in the event rate, due to electromagnetic scattering of the target electrons. The total cross section for single-photon exchange dipole scattering of electrons by neutrinos of energy E_ν is

$$\sigma^{\mathrm{EM}}(E_\nu) = f^2\pi r_0^2[(T/E_\nu) - \ln(T/E_\nu) - 1]\,, \qquad (10)$$

where T is an effective low-energy threshold on the recoil electron and is assumed large compared to m_e, r_0 is the classical electron radius ($r_0 = 2.82 \times 10^{-13}$cm), and f is the ratio of the neutrino electromagnetic moment to the electron Bohr magneton. This experiment observes neutrino-electron scattering of both muon and electron neutrinos at energies intermediate between reactor ($\overline{\nu}_e$, $E_\nu \approx 1 - 5$ MeV) and high-energy accelerator (ν_μ, $\overline{\nu}_\mu$, $E_\nu > 1$ GeV) neutrino sources. Limits are obtained [14] that on the electron-neutrino magnetic moment corroborate bounds from a reactor antineutrino experiment [15], and that on the muon-neutrino magnetic moments are more restrictive than any previous laboratory bound [12].

It is also possible to place bounds on anomalous contributions to the Lorentz and Dirac structure of the scattering amplitude, which would be manifest as changes in the expected electromagnetic form factors [16]. At low-momentum transfer, it is useful to discuss this effect in terms of an effective neutrino charge radius [17]. An intrinsic neutrino-charge radius, indicating the internal structure of a nonelementary neutrino, would be manifest as a shift δ of the weak neutral-current vector coupling, $g_V \to g_V + 2\delta$. Other shifts due to radiative corrections within the SM are predicted to be small, only ≈ -0.004 [17]. An intrinsic charge radius $\langle r^2\rangle$, however, introduces a radiative shift[1] $\delta = (\sqrt{2}\pi\alpha/3G_F)\langle r^2\rangle$ $= (2.39\times10^{30}\mathrm{cm}^{-2})\,\langle r^2\rangle$. Therefore, even if one conservatively assigns the entire shift $2\delta = g_V - g_V$ to anomalous effects, measurement of g_V in elastic scattering [18] may provide a very sensitive test of the internal electromagnetic structure of the neutrino down to a scale of 10^{-17} cm.

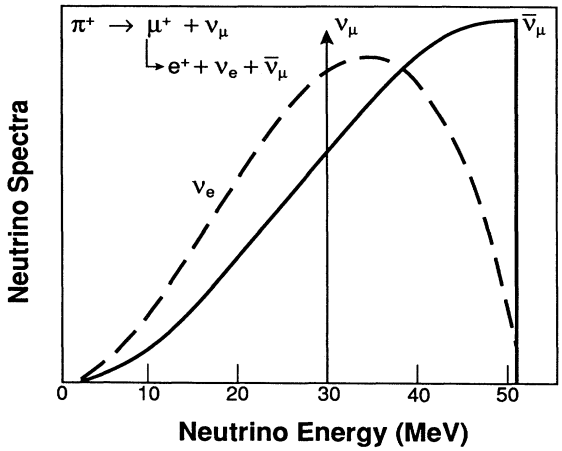

FIG. 3. Energy spectrum of neutrinos produced by π and μ decay at rest in the proton beam stop. Spectra for all three neutrinos are shown.

II. EXPERIMENTAL DESIGN

This experiment was performed at the Clinton P. Anderson Meson Physics Facility (LAMPF) using neutrinos produced in the proton beam stop. The neutrino detector was located in a well-shielded building placed at 90° to the proton beam and separated by over 6.3 m of steel from the beam stop neutrino source. The LAMPF beam stop neutrino source is described in the next section. The neutrino detector [19] included a 15-metric-ton active central detector with tracking and calorimetry, surrounded by multiwire proportional chambers (MWPC's) for active anticoincidence of incoming cosmic-ray particles, as described in Sec. II B.

A. Beam stop neutrino source

The LAMPF beam stop is a 12-kCi source of ≈30 MeV electron neutrinos. Neutrinos are emitted isotropically by pion decay at rest, followed by muon decay at rest, in the 800 MeV proton beam stop. Because the beam stop is compact, the neutrino source subtends less than 2° at the detector and can be treated as a point source. The neutrino spectra, shown in Fig. 3, are determined by the kinematics of the two-body $\pi^+ \to \mu^+\nu_\mu$ decay and the well-known three-body kine-

[1]There is an alternative definition of $\langle r^2\rangle$ that differs by a factor of 2 from that used here. See the discussion in Ref. [18].

matics for $\mu^+ \rightarrow e^+\nu_e\overline{\nu}_\mu$. Each stopped pion produces one of each neutrino $(\nu_e, \nu_\mu, \overline{\nu}_\mu)$. The LAMPF beam structure, 750-μs beam spills repeated at 120 Hz, does not allow the pion-decay neutrinos to be separated from the muon-decay neutrinos by event timing information. Nuclear absorption of stopped π^- and μ^- in the dense beam stop material and shielding suppresses production of $\overline{\nu}_e$ from μ^- decay by 5×10^{-4} relative to μ^+ decay to ν_e.

The absolute neutrino intensity is determined by the product of the incident proton current and the rate of stopped pion decays per proton, π^+/p. The proton current was measured by two precision calibrated toroidal induction monitors whose accuracy is better than 2%. The stopping pion production π^+/p was determined by a Monte Carlo calculation of proton and pion interactions in the LAMPF beam stop [20]. This Monte Carlo program was calibrated by an experimental measurement of π^+/p as a function of material and energy in a simplified, instrumented proton beam stop [21].

The calibration experiment measured the stopped-π^+/p ratio, in several materials, for proton energies that span the range encountered at the LAMPF beam stop. Protons were incident on a segmented beam stop composed of target material and thin plastic scintillators; the number of pion decays per incident proton was measured as a function of depth into the beam stop. Figure 4 shows the results for a typical calibration beam stop configuration; the solid line in the figure represents the output from the Monte Carlo calculation described below. The measured differential stopped-pion distribution was summed over depth to determine the total pion production per incident proton; results for the calibration experiment are summarized in Table I.

An *ab initio* Monte Carlo calculation [20] of proton and pion interactions in the beam stop is used to estimate the total neutrino production. To obtain the good agreement shown in Fig. 4, only two scaling factors (and no energy or atomic number dependences) have been applied to the relevant nuclear reaction data. Both adjustments are well within the experimental uncertainties of the data: the overall proton-nucleus reaction cross section was adjusted by 10% to reproduce the shape (dropoff with depth into the beam stop) of the measured π^+/p rate, and the total pion production cross section was rescaled by $\approx 10\%$ to get the best fit to the six calibration points listed in Table I. The final column of Table I shows the ratio of predicted-to-measured stopped-pion rates for the calibration beam stops; the agreement between data and scaled Monte Carlo simulation is better than the independent errors for each and every data point.

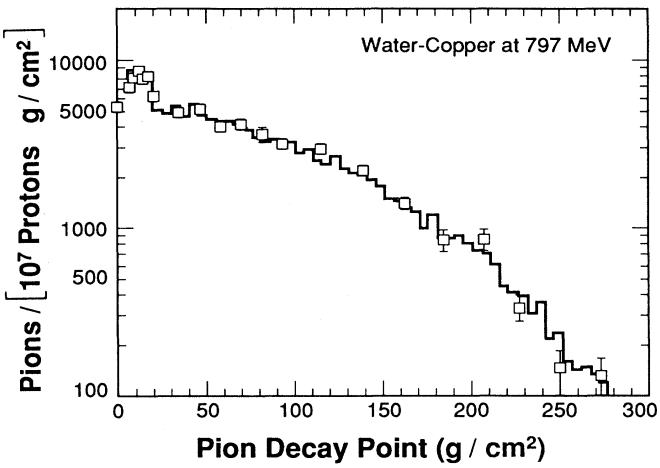

FIG. 4. Measured pion production rate in an instrumented beam stop. The solid line is the scaled Monte Carlo calculation; the initial bump in the data and calculation is due to 20 cm of water in the beam stop configuration.

This normalized Monte Carlo simulation was then used to simulate the results of the actual beam stop source. The LAMPF beam stop consisted of a 50-cm water-cooled copper stop, preceded by 0–9 aluminum target boxes containing isotope production targets and, for most of the experiment, a water-filled 20-cm-long beam degrader. The simulation accounted for the time-dependent changes in the running conditions, including short-term

TABLE I. The production of stopped pions per incident proton for various calibration beam stop configurations. A 5.9% systematic normalization uncertainty common to all six calibration points has been factored out to obtain the uncorrelated error used to weight the fit of the Monte Carlo result to the calibration data. The ratio of the normalized Monte Carlo simulation to the measured data is shown in the final column.

Material/proton energy	π^+/p (%)	Uncorrelated errors (%)	Monte Carlo/data
Copper and water			
797 MeV	8.40 ± 0.65	4.7	1.007
766 MeV	7.61 ± 0.74	7.6	1.048
Copper			
797 MeV	6.74 ± 0.53	5.1	0.978
766 MeV	6.02 ± 0.50	5.5	1.024
716 MeV	4.87 ± 0.45	6.6	0.998
Lead			
797 MeV	3.91 ± 0.35	6.4	0.969

changes in the number of isotope production target boxes inserted at the beam stop, to properly normalize the total neutrino production.

The total integrated proton current incident on the beam stop was $(1.12 \pm 0.02) \times 10^{23} p$, corresponding to the production of $(9.29 \pm 0.68) \times 10^{21} \nu_e$ at the source. At the detector, located at a $1/r^2$-weighted mean distance of 898.5 cm from the beam stop, the total integrated neutrino exposure was $(9.16 \pm 0.67) \times 10^{14} \nu_e/\text{cm}^2$.

The contributions to the uncertainty of the neutrino intensity are listed in Table II. Systematic uncertainties in the overall absolute normalization of the π^+/p calibration experiment account for the largest source of error, followed by uncertainties in the time-dependent composition of the actual LAMPF beam stop. The ability of the Monte Carlo simulation to reproduce the energy and atomic number dependence of the π^+/p calibration, as shown in Table I, is conservatively estimated to lead to an additional 2.4% error. All the contributions of Table II are added in quadrature to give a total uncertainty in the absolute neutrino exposure of 7.3%.

B. Detector apparatus

The neutrino detector consisted of a fine-grained tracking calorimeter (the "central detector") surrounded by massive shielding and high-efficiency cosmic-ray anticoincidence counters. Details of the construction [22, 23] and performance [19] of the detector have been published previously.

The central detector was composed of 40 repeated close-packed layers of plastic scintillation planes and flash chamber modules (FCM's). Each plane of plastic scintillator was divided into four separate 75 × 305 × 2.5 cm^3 counters viewed by a single photomultiplier. The pulse height in each individual scintillation counter, corrected for track position within the counter, was used to measure the dE/dx of particles traversing the detector; the sum of energy deposited in all counters was used to determine the "visible energy." Figure 5(a) shows the dE/dx for electrons measured in calibration triggers on stopped-muon decay; the total visible energy of the μ-decay electrons is shown in Fig. 5(b). The visible energy was roughly 60% of the total energy deposited within the detector, with the remainder being lost in the FCM's.

TABLE II. Sources of error in absolute neutrino intensity calculation.

Source of uncertainty	Error (%)
Systematic effects in calibration experiment	5.9
Fit of Monte Carlo calculation to all 6 calibration points	2.4
Simulation of actual beam stop configuration	3.0
Number of protons on target	2.0
Proton beam energy uncertainty	0.3
Distance between source and detector	0.5
Total uncertainty (quadrature sum)	7.3

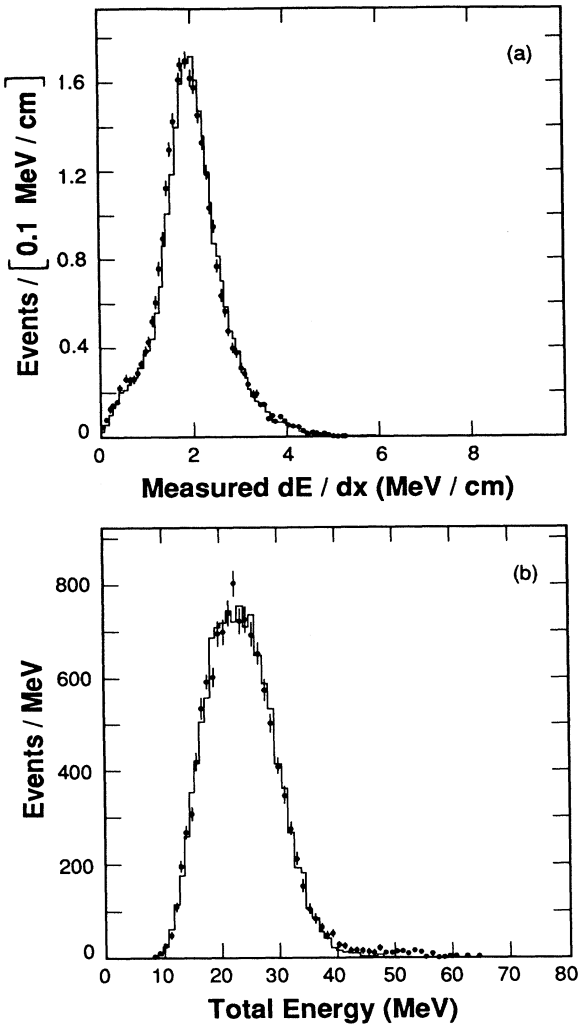

FIG. 5. Energy and dE/dx measurements of stopped muon-decay electrons within the central detector. Points with errors are measured data, the histogram is the Monte Carlo simulation. (a) Measured dE/dx in middle counters. (b) "Visible energy"-sum of energy deposited in all scintillation counters.

The FCM's were composed of extruded plastic panels, with 520 0.5 × 0.6 × 305 cm^3 helium-neon gas-filled tubes per panel. Five horizontally and five vertically oriented panels were alternated per module. The FCM's were used to provide track angle and location information for charged particles in the detector. Operational details have been published previously [23].

Active anticoincidence was necessary to discriminate against cosmic-ray-induced interactions which occurred at a rate of 10^8 per day, compared to the νe^- elastic scattering event rate of about one per day. The anticoincidence shield was composed of 594 multiwire proportional chambers (MWPC's) arranged in four layers on the walls and roof surrounding the central detector. A cosmic-ray veto signal (VETO) from the MWPC's would disable the detector for 20 μs whenever counters on two or more layers of any wall (or roof) detected signals in coin-

cidence. The VETO reduced the cosmic-ray trigger rate from 2 kHz to 0.07 Hz while introducing a dead time of about 12%. In order to distinguish events due to the decay of long-lived muons that stopped within the detector volume, the event history in each MWPC, and the energy deposited in each scintillation counter was recorded for 33.3 μs prior to each trigger.

Data were collected with a loose trigger that required a coincidence of scintillation counters on three or more consecutive layers, each with energy deposit loosely consistent with that expected from a single minimum-ionizing particle, and no cosmic-ray VETO. The energy requirements included an upper limit at roughly 18 MeV ($\sim$ 3 times the minimum ionizing) in any single scintillation counter in order to eliminate triggers due to energetic proton recoils from np elastic scattering. The thresholds on individual scintillation counters, in combination with the energy lost in the FCM's between the scintillator layers, imposed an effective trigger threshold of about 14-MeV kinetic energy for electrons traveling normally to the detector planes.

Triggers were obtained during the LAMPF beam spill (beam-ON), which lasted 750 μs with repetition rate of 120 Hz. About two-thirds of all triggers collected during the beam-ON period were due to cosmic-ray-induced interactions. Therefore cosmic-ray-induced data (beam-OFF) were collected for a period approximately four times longer between beam spills. The beam-OFF data were analyzed identically to the beam-ON data and were used to determine, and then to statistically subtract, the cosmic-ray backgrounds in the final data sample.

III. DATA ANALYSIS

A total of 562 739 beam-OFF and 223 751 beam-ON triggers were collected during 2049.5 h of beam-OFF and 550.2 h of beam-ON live time. Only about 1% of the beam-ON triggers were expected to be due to neutrino interactions in the detector. The vast majority were induced by cosmic rays and beam-associated neutrons traversing the detector. The signal-to-noise ratio for neutrino scattering was enhanced by a selection of events that had the energy and track characteristics expected for single electrons and that were not associated with secondary interactions prior to or during the trigger time period; it should be noted that no explicit cuts were made on the electron angle. Table III lists the selection criteria along with the reduction in the data sample and the loss of detection efficiency for $\nu_e e^-$ scattering imposed by each cut. These restrictions are described below.

Actual cut values used to winnow the data were generally selected on the basis of the effect upon the beam-OFF data set, and upon a large sample of electrons in stopped-muon decay calibration triggers. The reduction in experimental sensitivity to the scattering signal inflicted by each of the restrictions and cuts was evaluated by means of a detailed Monte Carlo simulation of the detector response to $\nu_e e^-$ elastic scattering events. The EGS4-based [24] simulation included a complete emulation of the track and energy measurements based on a very large sample of calibration measurements and calibration triggers interspersed with the main data sample.

TABLE III. Measured reduction of the data sample and calculated loss of detection efficiency for various restrictions. Quantities in parentheses refer to the beam-associated fraction of the beam-ON data. The event numbers in the bottom two lines result from fits to the data as described in Sec. IV.

Selection criteria	2049.5 h Beam OFF	550.2 h Beam ON	$\nu_e e^-$ Detection efficiency
Triggers	562 739	223 751	0.263
Reconstructed track	$\times$0.65	($\times$0.14)	$\times$0.83
Inside fiducial volume	$\times$0.38	($\times$0.90)	$\times$0.88
No pretrigger act. in veto or scint.	$\times$0.56	($\times$0.92)	$\times$0.95
Visible energy and track length cut	$\times$0.74	($\times$0.93)	$\times$0.99
No obvious backgrounds	59 088	26 892	0.198
$dE/dx \leq 1.85$ mips	$\times$0.58	($\times$0.41)	$\times$0.96
Electron/γ sample	34 613	13 416	0.193
Hits in both views of first FCM	$\times$0.77	($\times$0.53)	$\times$0.98
One or two scint. groups	$\times$0.82	($\times$0.93)	$\times$0.98
Electron sample	21 773	7 752	0.187
Electron direction	$\times$0.94	($\times$0.98)	$\times$0.98
$dE/dx > 0.5$ mips	$\times$0.92	($\times$0.95)	$\times$0.98
Track quality/location/energy ($\mathcal{S}$)	$\times$0.55	($\times$0.68)	$\times$0.90
νe^- elastic scattering data set	12 953	4 880	0.164
νe^- events	295 ± 35		
$\nu_e e^- \rightarrow \nu_e e^-$ events	236 ± 35		

"Synthetic data" sets were produced in the same format and analyzed with the identical codes as were the measured data. To simulate the effects of noise in the tracking chambers, MWPC VETO system, and scintillation counters, activity from calibration triggers was overlaid on the synthetic data.

The data analysis began with a least-squares straight-line fit of hit FCM tubes in each event to determine the track location and direction. Approximately 85% of the beam-associated triggers failed the track-fitting-procedure and were rejected. Inefficiencies in the tracking system were estimated to cause a loss of 17% of the neutrino-electron scattering triggers. Each event was required to be contained within the detector by eliminating events that had tracks that extended to within 5 cm of the FCM edges, or that had energy deposit in the first or last scintillation layer, thereby removing about 12% of the elastic scattering events, and more than 60% of the cosmic-ray-induced triggers.

Events were also removed if there was excessive activity in either the scintillation counters or MWPC's during the pretrigger period indicating the presence of stopping muons. Figure 6 demonstrates the time history of activities in the anticoincidence system and in the scintillation counters. The sharp peak in the MWPC activity near the trigger time is due to leak-through cosmic-ray events for which the VETO arrived after the trigger decision. These events are removed by imposing the hardware VETO conditions in software. The exponential rise in scintillator activity at short times represents triggers on muon-decay electrons, arising from inefficiencies in the MWPC shield; they are removed by eliminating all events with energy deposit greater than 3 MeV in any scintillation counter in the 20 μs prior to the trigger. The increase in activity at times earlier than 20 μs are due to stopped muons which decayed after the on-line VETO was lifted; the subsequent decay electron was removed by eliminating any event, which had energy deposit > 1 MeV in any counter adjacent to the trigger scintillators during the time $20 < t < 33$ μs prior to the trigger. The net effect of these "pretrigger" restrictions is to reduce the signal detection efficiency by approximately 6% due to overlap of random activities with the trigger event.

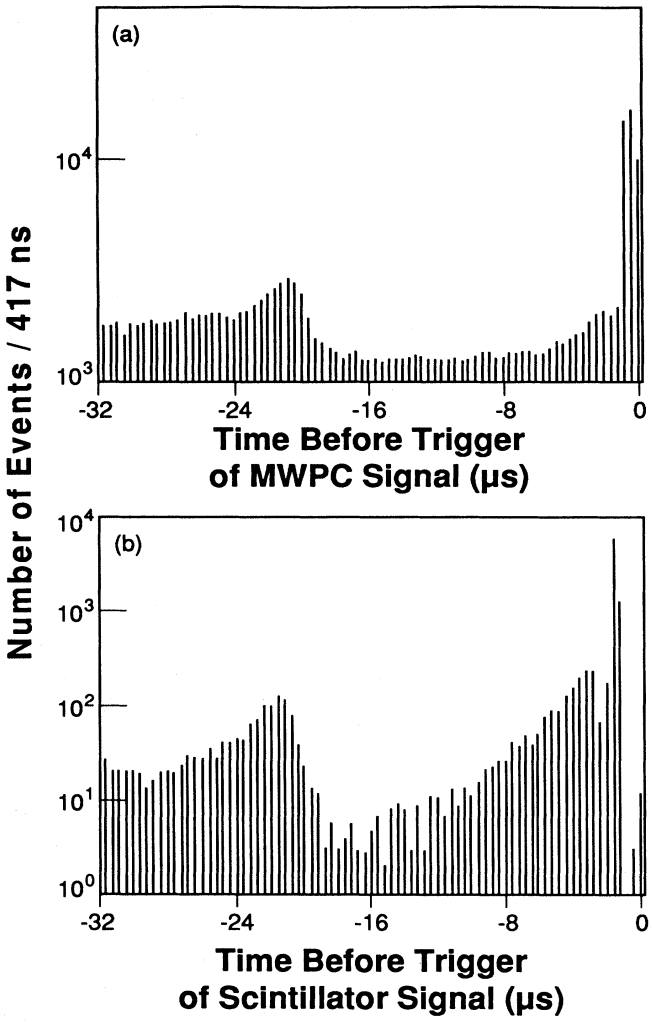

FIG. 6. Histogram of time of activity relative to trigger event. (a) Signals in MWPC system. (b) Energy deposit in scintillation counters.

To define uniquely the kinematic thresholds in the analysis, events were required to have a primary track length between $3 \leq L \leq 7$ scintillation planes, and to have visible energy in the range 7 MeV $< E_{\rm vis} <$ 60 MeV. The application of the above simple cuts, applied in parallel, reduced the data sample by a factor of 10, while retaining more than 70% of the neutrino-induced triggers. A large fraction of events in the remaining data sample were presumably caused by neutron-induced γ-ray production. Figure 7 shows the dE/dx distribution of the beam-associated data sample at this stage, for all scintillation counters excluding counters at either end of the trigger event. The distribution exhibits a broad minimum-ionizing-particle peak (single electrons), and a bump at twice-minimum-ionizing and higher energies due to pair conversion (e^+e^-) and residual highly ionizing particles, such as stopping pions or recoil protons. To enhance the fraction of single-electron events, a cut was applied as indicated by the vertical line in Fig. 7, which required less than 3.85 MeV/g cm^2 or about 1.85 minimum-ionizing particles, in any of the middle scintillation counters. This dE/dx particle identification removed more than half of the beam-associated background at the cost of a 4% reduction of the neutrino-event rate.

Electrons from neutrino interactions are expected to leave just one well-defined track, whereas neutrons frequently have multiple interactions. Thus, events were eliminated if there were more than two groups of contiguous scintillation counters and if there were not at least one tube hit in both views of the FCM nearest to the beam stop. These two restrictions were particularly effective at eliminating neutron-induced events, so that 50% of all beam-associated (and 20% of all cosmic-ray) events were thrown away, while 96% of the remaining neutrino-electron scattering events were retained. By accepting

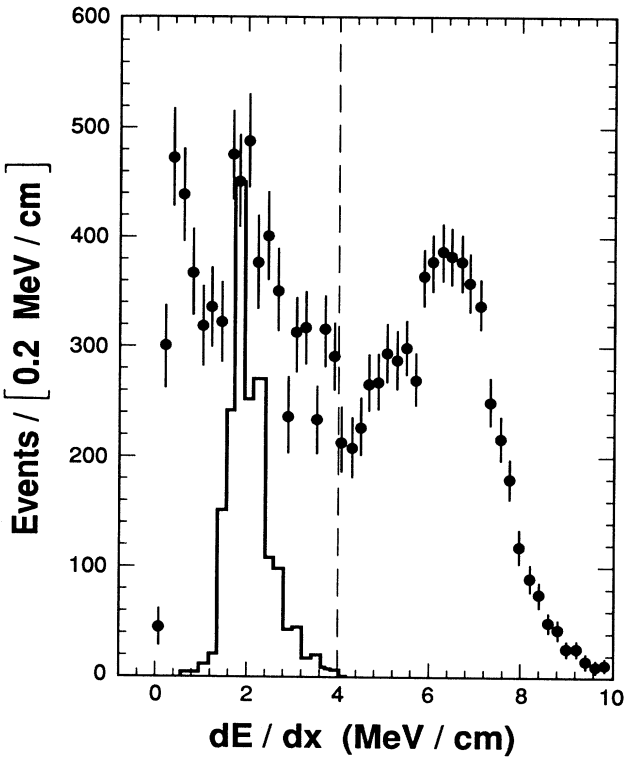

FIG. 7. dE/dx for the beam-associated data. The histogram represents the expected νe^- signal; events with dE/dx above the vertical line were eliminated.

events with two groups of scintillation counters, we maintained good efficiency for single electrons even if accompanied by bremsstrahlung radiation; approximately 8% of all $\nu_e e$ events were expected to radiate a photon producing a second group of scintillation counters above 1.5 MeV threshold, whereas fewer than 1.5% were expected to have three or more such clusters.

The remaining data set of 7752 beam-ON events contained 2100 beam-associated events, about a third of which were likely caused by neutron, not neutrino, interactions. The final set of selection criteria were of necessity somewhat more subtle than the preceding requirements. First, to eliminate an apparent small tail in the data at low dE/dx that was not consistent with measured electron distributions from stopped-muon decay, events were eliminated if any middle scintillation counter recorded $dE/dx < 1.15$ MeV/g cm^2 (0.55 minimum ionizing particles). Second, a cut was made to favor events with electrons travelling in the "forward" hemisphere. The absolute track direction had a backward and/or forward ($\cos\theta \leftrightarrow -\cos\theta$) ambiguity, so this cut relied on bremsstrahlung radiation to indicate the primary particle direction. For an event with two sets of hit scintillators, it is presumed that the higher-energy cluster is due to the primary electron because of the preference to radiate lower-energy photons. Therefore, any event with two groups of scintillators for which the "downstream" (further from the beam stop) group had more than two scintillation layers was eliminated. Roughly half of the 10% of cosmic-ray events with two scintillation groups were removed.

Finally, a selection criterion to eliminate events that are correlated with the tails of distributions, based upon the track fit quality and track location, was applied; it removed about half of the residual neutron events at the cost of 10% of the remaining neutrino-induced signals. A likelihood parameter $\mathcal{S}$ was computed for each event according to $\mathcal{S} = \chi^2_{\rm fit}[dE/dx|_{\rm max} - \langle dE/dx\rangle]/D_{\rm min}$. Here, $\chi^2_{\rm fit}$ is the reduced χ^2 statistic for the fitted track, $D_{\rm min}$ is the distance from the track end point to the nearest edge of the detector, $dE/dx|_{\rm max}$ is the largest dE/dx measured in a middle scintillator, and $\langle dE/dx\rangle$ is the average over the entire data sample. Figure 8 shows the $\mathcal{S}$ distribution of the data compared to the Monte Carlo estimate for the elastic scattering signal. The final cut was selected to keep about 90% of the elastic scattering signal as shown

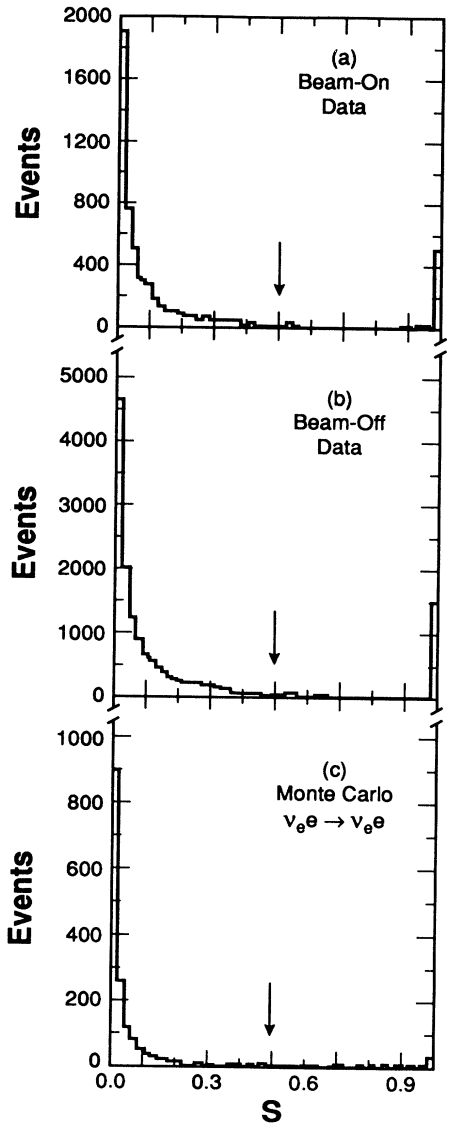

FIG. 8. Distribution of $\mathcal{S}$ in measured data and Monte Carlo sample of $\nu_e e^-$ events. The normalization of the $\nu_e e^-$ sample is arbitrary.

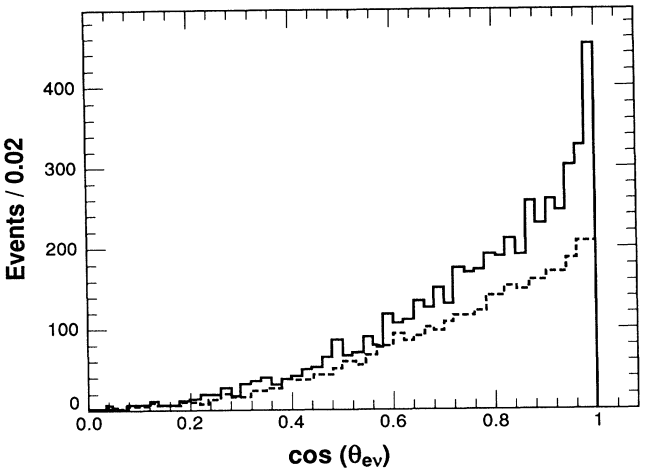

FIG. 9. Angular distribution for the final beam-ON data set. The normalized cosmic-ray data taken during beam-OFF are shown as a dotted line.

in Fig. 8.

The angular distribution of the remaining 4880 beam-ON events is displayed in Fig. 9. The normalized distribution of cosmic-ray-induced events (beam-OFF data) is shown as a dotted line. The beam-associated event rate is $4880 - (12\,953/3.83) = 1492 \pm 76$ events, where the weighted beam-OFF/beam-ON livetime ratio R=3.83. The measured visible energy and recoil-angular distributions of the beam-associated event sample, obtained by subtracting the scaled cosmic-ray data bin by bin, are shown in Fig. 10. The clear excess of events at the most forward angles in Fig. 10 is the unambiguous signal of neutrino-electron elastic scattering events.

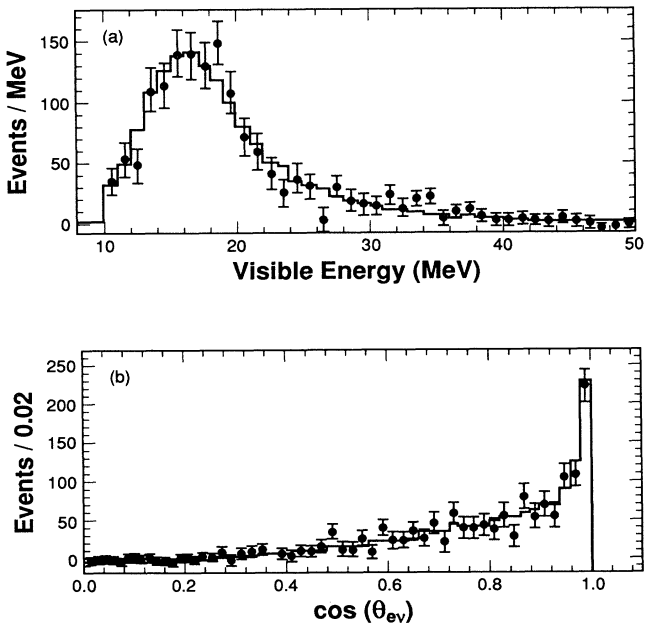

FIG. 10. Distribution of recoil angle $\cos\theta_e$ and visible energy $E_{\rm vis}$ for beam-associated events. The solid line is the result of the best fit to the data.

IV. NEUTRINO-ELECTRON SIGNAL

After all the restrictions were applied, the remaining 4880 beam-ON events consisted of electrons produced by neutrino interactions as well as residual cosmic-ray- and neutron-induced events. The contribution from cosmic rays is determined from the beam-OFF data. The observed beam-associated distributions shown in Fig. 10 are assumed to be the sums of contributions from the neutrino-electron scattering signal, plus neutrino-induced backgrounds from charged-current scattering on ^{12}C, from charged-current reactions with other elements in the detector (designated as ^{13}C), and also from neutron-induced γ rays.

A. Distributions used in the fit to extract νe^- signal

The elastic scattering signal is extracted by a multiparameter maximum-likelihood fit to the observed kinematic distributions of visible energy $E_{\rm vis}$ and recoil angle $\cos\theta_{e\nu}$. The object of the fit is to determine the relative contribution from each of the sources (νe^-, ν_e ^{12}C, ν_e ^{13}C, neutrons). The shape of the distributions expected for each of these contributions is determined by a detailed simulation of the detector response to electrons and gamma rays. Figure 11 shows the calculated angular and visible energy distributions for the components of the final event sample. Of all of the interactions consid-

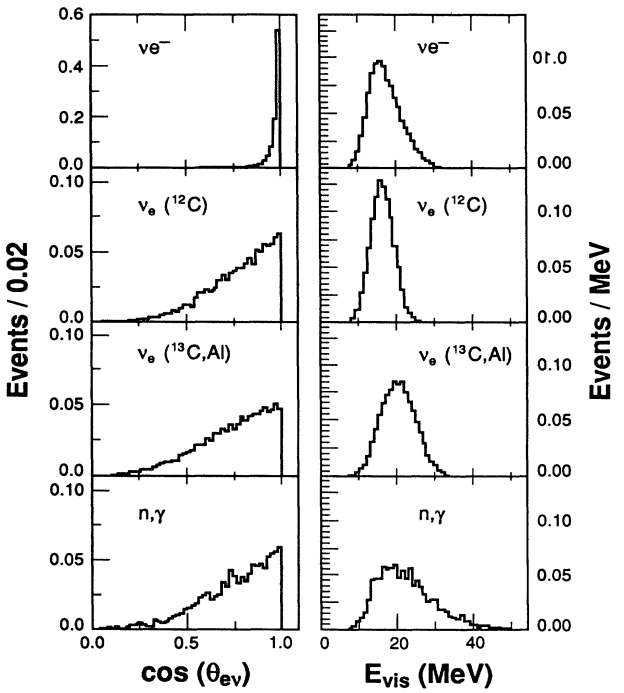

FIG. 11. Calculated Monte Carlo distributions of energy and angle for neutrino-electron scattering, and neutrino-carbon, neutrino-nuclear, and neutron-induced background events. The distributions are normalized to unity. The vertical scale is changed for the elastic scattering angular distribution.

TABLE IV. Sources of events in the final data sample. The fourth row represents neutron-induced γ-ray background events, and the entire final column is the result of the fit described in Sec. IV B. The "expected rate" is evaluated for a neutrino flux $\phi = 9.16 \times 10^{14}$ cm^{-2}.

Reaction	Targets T ($\times 10^{29}$)	$\langle\sigma\rangle$ 10^{-42} cm^2	$\langle\epsilon\rangle$ (%)	Expected rate	Best fit
$(\nu_e + \nu_\mu + \overline{\nu}_\mu)e^-$	49.5	0.4	15.7	284	295 ± 35
ν_e ^{12}C	6.36	13.2	7.6	583	626 ± 71
ν_e(^{13}C + ^{27}Al)	0.17	103.2	17.6	282	136 ± 102
$n\gamma$					435 ± 90

ered, only neutrino-electron scattering results in a highly peaked angular distribution.

For νe^- scattering, events were generated according to differential distributions appropriate for $\sin^2\theta_W = 0.23$ and include all three neutrino types in the beam ($\nu_e, \nu_\mu, \overline{\nu}_\mu$). The final results are insensitive to the value of $\sin^2\theta_W$, and to the admixture of ν_μ and $\overline{\nu}_\mu$, chosen for the simulation because the forward peaking of the elastic scattering angular distribution evident in Fig. 11 is a kinematic fact of life and, given our experimental resolution, not sensitive to the dynamics.

Neutrino-nuclear reactions were simulated with differential cross sections supplied by Donnelly [25] for specific nuclear transitions, e.g., ^{12}C$(\nu_e, e^-)^{12}$N(gs), and then summed over all transitions, where gs denotes the ground state. The fitting procedure explicitly separated the ^{12}C contribution from reactions on other nuclei, because the higher threshold for ν_e ^{12}C charged-current reactions results in significant differences between the recoil electron spectra. Table IV lists the appropriate quantities for the number of targets (T), spectrum-averaged event detection efficiency ($\langle\epsilon\rangle$), and calculated beam-averaged cross sections ($\langle\sigma\rangle$) for the neutrino-induced processes. These quantities are combined to obtain the expected event rate $R = \langle\epsilon\rangle\langle\sigma\rangle\phi T$ listed in the fourth column.

The neutron-induced γ rays were generated [26] according to a rapidly falling spectrum appropriate for $np\gamma$ (bremsstrahlung) and radiative neutron capture on protons, plus a smaller contribution peaked near 20 MeV as expected for giant-resonance capture. The intrinsic angular distribution was approximated as isotropic in the center of mass.

The elastic scattering signal was extracted using a binned maximum-likelihood fit to the observed angular and visible energy ($\cos\theta_{e\nu}, E_{\rm vis}$) correlated distributions. The data were sorted into 323 bins ($17\cos\theta_{e\nu} \times 19E_{\rm vis}$, with unequal spacing) and fit with the likelihood function

$$\mathcal{L}(R_k) = \Sigma_{i=1}^{323}[2(N_i^{\rm fit} - N_i^{\rm obs}) + 2N_i^{\rm obs}\ln(N_i^{\rm obs}/N_i^{\rm fit})] \,. \quad (11)$$

Here, $N_i^{\rm obs}$ is the observed event rate in bin i and $N_i^{\rm fit} = \Sigma_k R_k f_k(i)$ is the expected event rate in bin i given a total of R_k events from process k [$k = \nu e^-, \nu_e$ ^{12}C, ν_e ^{13}C, $n\gamma$, cosmic ray (CR)]. The distributions $f_k(i) = f_k(\cos\theta_{e\nu}, E_{\rm vis})$ were taken from detailed Monte Carlo simulations. R_k are the free parameters of the fit, and the total number of events ($\Sigma_k R_k$) is fixed to match the observed data sample. To eliminate bins with negative population, the fit is performed to the beam-ON data without subtracting the beam-OFF (CR) contribution. The CR contribution is included in the fit, but its normalization ($R_{\rm CR}$) is fixed. Spline fits to the beam-OFF data are used as the CR component in the likelihood fit in order to reduce sensitivity to statistical fluctuations in the finite beam-OFF data set.

B. Fit results and tests

The rightmost column of Table IV shows the normalization of each beam-associated contribution obtained from the maximum likelihood. The result is plotted as the solid line on top of the data in Fig. 10. The measured νe^- event rate is 295 ± 35 events. The quoted error is dominated by the statistical uncertainty implied by the presence of the large cosmic-ray background in the forward angular bins, as shown in Fig. 9 and discussed above. Within the quoted statistical errors on the other components, there is good agreement between calculated background rates and the fit results. In the case of the ν_e ^{12}C reaction, which is the largest single source of beam-associated background, there is good agreement between the fit result and an independent measurement relying solely on the observation of the ^{12}N(gs) decay [27]. The neutron-induced event rate is within a factor of 2 of the expectations from an absolutely normalized calculation of neutron propagation and attenuation by $\sim 10^{-15}$ through the beam stop shielding [26]. Figure 12

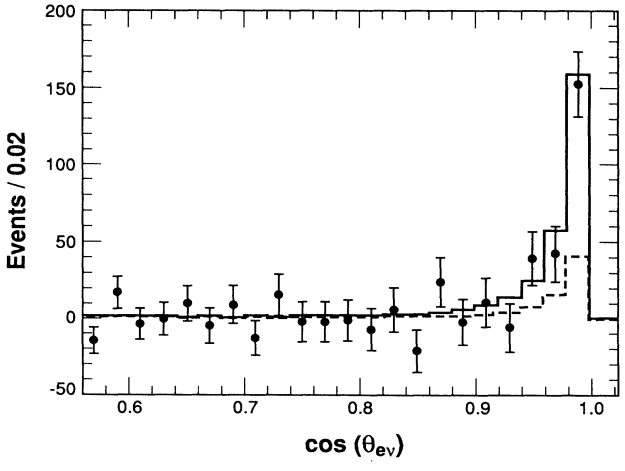

FIG. 12. Angular distribution of the measured elastic scattering signal. The solid line is the result of the best fit, 295 ± 35 events. The dotted line is the background contribution from the 59.2 $(\nu_\mu + \overline{\nu}_\mu)e^-$ scattering events.

TABLE V. Comparison of fit results for different hypotheses about the source of events contributing to the final event sample. A blank line indicates the source is neglected completely. The cosmic-ray contribution is fixed except when shown with ± errors.

event ‖ fit → / Type ‖ type →	Best fit	C.R. rate unconstrained	No neutron contribution	No ν_e CC on ^{13}C	Fit $\cos\theta_{e\nu}$ only
χ^2/N_{DF}	413/320	413/319	440/321	415/321	9.3/13
νe^-	295 ± 35	293 ± 36	317 ± 38	295 ± 35	297 ± 37
ν_e ^{12}C	626 ± 71	600 ± 87	660 ± 72	671 ± 94	50 ± 236
$\nu_e(\ ^{13}C + \cdots)$	136 ± 102	122 ± 102	515 ± 69		702 ± 211
Neutron-induced γ	435 ± 90	396 ± 115		526 ± 62	442 ± 239
Cosmic ray	3388	3470 ± 162	3388	3388	3388

shows the angular distribution of the elastic scattering signal remaining after all beam-associated and cosmic-ray backgrounds have been subtracted.

The results for the νe^- scattering rate are stable against changes in the assumed distributions of the background components because only elastic scattering produces a sharply peaked angular distribution. Table V summarizes the results of alternative fits, which were used to check against systematic biases in the fitting procedure. Even when the fit is attempted with the extreme assumption that one of the less well-understood background components can be neglected completely, the result for the νe^- signal rate is only marginally affected. This same insensitivity occurs if the CR contribution is allowed to be a free parameter of the fit. The final column of Table V shows that a fit to only the angular distribution gives results in very good agreement with the complete fit.

Other systematic studies showed that the νe^- rate is also insensitive to changes in the bin sizes and boundaries, ranges of energy or angle, and changes in the weighting algorithm (maximum likelihood or least squares) used. Therefore, we estimate that the "statistical" error returned from the fit, ±35 events, is sufficient to cover the systematic uncertainties associated with the entire fitting procedure.

C. Subtraction of elastic scattering backgrounds to $\nu_e e^-$ signal

The measured event rate $R(\nu e^-) = 295 \pm 35$ events include background contributions from $\nu_\mu e^-$ and $\overline{\nu}_\mu e^-$ elastic scattering. This background can be estimated, in a model-independent method, through use of measured cross sections. The absolute cross sections [11,12], $\sigma(\nu_\mu e^-)/E_\nu = 1.90 \pm 0.28 \times 10^{-45}$ cm^2/MeV and $\sigma(\overline{\nu}_\mu e^-)/E_\nu = 1.25 \pm 0.19 \times 10^{-45}$ cm^2/MeV, and experimental detection efficiencies determined by Monte Carlo simulation, lead to 27.7 ± 4.1 $\nu_\mu e^-$ events and 31.5 ± 5.1 $\overline{\nu}_\mu e^-$ events. Although the $\nu_\mu e^-$ and $\overline{\nu}_\mu e^-$ detection efficiencies are functions of $\sin^2\theta_W$, the background contributions have an anticorrelated dependence, so that the sum of their event rates is almost independent of the value of $\sin^2\theta_W$ assumed in the analysis. Subtracting the background contribution of 59.2 ± 6.5 events from the total elastic scattering rate of 295 ± 35 leaves a net $\nu_e e^-$ signal of 236 ± 35 events.

V. PHYSICS RESULTS

A. The $\nu_e e^- \rightarrow \nu_e e^-$ total cross section and discussion of systematic uncertainties

The flux-weighted total cross section is measured from the observed event rate R, neutrino intensity ϕ, integrated target density T and experimental detection efficiency ϵ according to $\sigma = R/\epsilon\phi T$. The ultimate precision of the measurement of σ, or of theoretical parameters derived from σ, is influenced by the errors on each of the quantities on the right-hand side of this expression. The experimental value and estimated uncertainty for each term is listed in Table VI. The methods used to obtain these values and to estimate the associated uncertainties are described below, and then the quantities are combined to obtain the measured $\nu_e e^-$ elastic scattering cross section.

The "statistical" errors associated with the observed event rate, $R = 236 \pm 35$ events, were already discussed in the preceding section of this paper; similarly the "systematic" normalization uncertainty on the neutrino flux intensity, $\phi = (9.16 \pm 0.67) \times 10^{14}$ cm^{-2}, was summarized in Table II. The integrated target density, $T = (4.94 \pm 0.07) \times 10^{30}$ electrons, was determined from the measured mass and chemical composition of the detector materials; $(9.75 \pm 0.10) \times 10^6$ g of polystyrene plastic scintillator ($CH_{1.10}$), $(3.93 \pm 0.05) \times 10^6$ g polypropylene FCM extrusions (CH_2), and $(1.31 \pm 0.03) \times 10^6$ g of other material, mostly aluminum for equipotential planes. The total uncertainty in the integrated electron thickness is about 1.5%.

The flux-weighted integrated detection efficiency ϵ for the signal reaction is determined with the same Monte Carlo simulation of detector response to electrons and γ rays previously described in relation to the fit functions. Figure 5 demonstrates the good agreement between the energy scale in the simulation and measured calibration data. Figure 13 shows a calculation of the angle with respect to the detector axis of electrons from muon-decay compared to measured muon-decay triggers,

TABLE VI. Values and uncertainties of quantities used to calculate absolute normalization of event rate and cross section.

Experimental quantity		Value	Uncertainty	
Observed event rate	R	236		
Multiparameter fit				14.7 %
$(\nu_\mu + \overline{\nu}_\mu)e^-$ backgrounds				2.9%
Total statistical error			δR	15.0%
Neutrino intensity ($\times 10^{14} \nu_e/\mathrm{cm}^2$)	ϕ	9.16		
(Table II)			$\delta\phi$	7.3%
Target thickness ($\times 10^{30} e^-$)	T	4.94		
Composition and mass			δT	1.5%
Detection efficiency	ϵ	0.164		
Tracking simulation				4.0%
Energy scale				3.1%
Pretrigger noise				1.0%
			$\delta\epsilon$	5.2%
Total systematic error				9.1%

also indicating the reliability of the detector simulation. The differential acceptance, $A(\cos\theta_{e\nu}, E_e)$, for electrons of fixed energy E_e and recoil angle $\cos\theta_{e\nu}$ is determined by simulation; generally the acceptance increases linearly as $\cos\theta_{e\nu}$ approaches 1, and at forward angles increases between $15 < E_e < 30$ MeV to an asymptotic value. The dependence on energy and angle over the entire range is parametrized [28] by an empirical four-component function with energy-dependent coefficients obtained by spline fits. With $A(\cos\theta_{e\nu}, E_e)$ known, the integrated detection efficiency ϵ is determined numerically according to

$$\epsilon = \frac{\int_0^{E_\nu^{\max}} \int_0^{E_e^{\max}} A(\cos\theta_{e\nu}, E_e)[d\sigma(E_\nu)/dE_e]\phi(E_\nu) dE_\nu dE_e}{\int_0^{E_\nu^{\max}} \sigma(E_\nu)\phi(E_\nu) dE_\nu}, \tag{12}$$

where $A(\cos\theta_{e\nu}, E_e)$ is the fractional acceptance for electrons with energy E_e traveling in direction $\cos\theta_{e\nu}$; $d\sigma(E_\nu)/dE_e$, $\sigma(E_\nu)$ is the differential and total cross section as a function of neutrino energy E_ν, and $\phi(E_\nu)$ is the neutrino spectrum (normalized to unity). This integral function is usually referred to simply as the "detection efficiency," although the integration and flux weighting is always implied; the expression in the denominator of Eq. (12) is referred to as the flux-weighted total cross section.

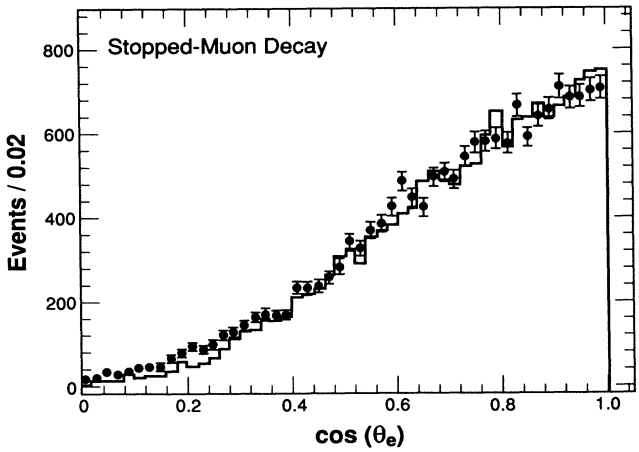

FIG. 13. Comparison of simulation and data, for muon-decay electron reconstructed track angle relative to the detector axis.

The systematic uncertainties in the detection efficiency are summarized in Table VI. These are determined empirically by the difference in calculated detection efficiencies when the simulation is repeated with the associated detector parameters (e.g., photoelectrons/MeV, FCM hit efficiency, etc.) varied to the extremes of measured calibration data. The efficiency is uncertain by up to 4% due to the tracking simulation, and by 3.1% due to uncertainties in the overall energy scale. The quoted uncertainties due to tracking and energy scale include detailed consideration of any apparent disagreements between the simulation and measured data. The loss of efficiency due to random overlap of uncorrelated noise with true elastic scattering events is determined with 1% uncertainty from a sample of 68 000 calibration triggers interspersed with the neutrino-trigger sample.[2] Combining the uncertainty in tracking, energy cuts and pretrigger activity restrictions, the total uncertainty of the calculated detec-

[2]For simulation purposes, "noise" information is extracted from these calibration events and inserted into random "synthetic" events.

tion efficiency is 5.2%.

An important simplification of the analysis in the following sections can be obtained by recalling that the differential cross section for elastic scattering, Eq. (2), can be broken down into the sum of two incoherent parts, the left-handed (uniform distribution) and right-handed $[d\sigma/dy = (1-y)^2]$ contributions. The integrated detection efficiency for the left-handed component obtained from Eq. (12) is $\epsilon_L = 0.168 \pm 0.008$, and for the right-handed component is $\epsilon_R = 0.037 \pm 0.002$. The experimental detection efficiency is much greater for the left-handed component due to the more energetic recoil electron spectrum.

The quantities in Table VI are combined to obtain the measured value for the (neutrino flux-weighted) elastic scattering cross section

$$\sigma(\nu_e e^-) = 3.18 \pm 0.48 \pm 0.29 \times 10^{-43} \text{ cm}^2 . \quad (13)$$

The elastic scattering cross section is proportional to the incident neutrino energy, so the flux-weighted cross section is equivalent to the total cross section for neutrinos with the mean beam energy $\langle E_{\nu_e} \rangle = 31.7$ MeV:

$$\sigma(\nu_e e^-)/E_\nu = 10.0 \pm 1.5 \pm 0.9 \times 10^{-45} \text{ cm}^2/\text{MeV} , \quad (14)$$

where the first error is statistical and the second is the systematic normalization uncertainty. The cross section can also be expressed as $\sigma(\nu_e e^-) = (2.32 \pm 0.35 \pm 0.21)\sigma_0$.

B. Model-independent measurement of NC/CC interference

The interference between the charged and neutral currents is measured by the difference between the total cross section and the sum of the charged and neutral cross sections. Using Eq. (7) to separate the helicity components, the total event rate is $R = T\phi(\epsilon_L \sigma^{\rm CC} + \epsilon_L \sigma^I + \epsilon_{\rm NC}\sigma^{\rm NC})$. For convenience, we define an experimental constant $\kappa = T\phi\sigma_0 = 618$ events. The charged-current cross section $\sigma^{\rm CC} = 4\sigma_0$ contributes $R^{\rm CC} = 4\epsilon_L\kappa = 416$ events to the total event rate. From Sec. I B, the neutral-current cross section is $(0.442 \pm 0.065)\sigma_0$. The detection efficiency $\epsilon_{\rm NC}$ is evaluated in a self-consistent way to be 0.152, so that the neutral-current contribution to the rate is $R^{\rm NC} = 0.442\epsilon_{\rm NC}\kappa$ or 41.5 ± 5.9 events. Therefore, the NC/CC interference contribution is obtained:

$$\begin{aligned} R^I &= R^{\nu_e e} - R^{\rm CC} - R^{\rm NC} \\ &= 236 \pm 35 - 416 - 41 \\ &= -221 \pm 35(\text{stat}) \pm 21(\text{syst}) . \end{aligned} \quad (15)$$

The stat error includes the statistical errors from the measured event rate and the experimental errors on the $\sigma^{\rm CC}$ and $\sigma^{\rm NC}$ cross sections added in quadrature. The syst error represents the 9.1% systematic normalization uncertainty on the $\nu_e e^-$ event rate (see Table VI). The interference contribution R^I is unambiguously destructive, about five standard deviations from zero. The interference contribution to the total cross section is $\sigma^I = -2.13\sigma_0$, where the interference coefficient is evaluated according to

$$I = \sigma^I/2\sigma_0 = R^I/2\epsilon_L\kappa = -1.07 \pm 0.21 . \quad (16)$$

As described in Sec. I B, the SM predicts for $\sin^2\theta_W = 0.23$ that $I = -1.08$; the agreement between experiment and the SM is dismayingly excellent.

Particularly in the case of more complex reactions, such as coherent trilepton production, the interference is sometimes expressed [29] in terms of a phase angle Φ between the charged-current amplitude $A^{\rm CC}$ and neutral-current amplitude $A^{\rm NC}$. In the case of the $\nu_e e^-$ elastic scattering cross section, we can identify the angle as

$$\begin{aligned} \sigma(\nu_e e^-) &= \sigma^{\rm CC} + \sigma^{\rm NC} + \sigma^I \\ &= ||A^{\rm CC}||^2 + ||A^{\rm NC}||^2 + 2A^{\rm NC}A^{\rm CC}\cos\Phi . \end{aligned} \quad (17)$$

Substitution of the "square root" of $\sigma^{\rm CC}$ and $\sigma^{\rm NC}$ to obtain the magnitude of the CC and NC amplitudes allows Eq. (17) to be solved as $\cos\Phi = -0.801 \pm 0.17$, $\Phi = 143^\circ\ ^{+23^\circ}_{-15^\circ}$. One way to visualize this phase is as the angle between the CC and NC amplitudes in the (L, R) helicity plane.

C. Measurement of $\sin^2\theta_W$

Assuming the standard model correctly describes the neutrino-electron cross section, we can evaluate the observed νe^- elastic scattering event rate R in terms of the single free parameter, $X_W = 2\sin^2\theta_W$:

$$R = \kappa\left(\epsilon_L(1+X_W)^2 + \frac{1}{3}\epsilon_R(X_W)^2\right) , \quad (18)$$

where $\kappa = \phi T\sigma_0 = 618$ events. Equation (18) can be reexpressed as a quadratic equation for X_W:

$$0 = (\epsilon_L + \tfrac{1}{3}\epsilon_R)X_W^2 + 4\epsilon_L X_W + (\epsilon_L - R/\kappa) . \quad (19)$$

Equation (19) is solved as $\sin^2\theta_W = 0.249$. The allowed range of $\sin^2\theta_W$ is evaluated by a Monte Carlo calculation, allowing the terms (ϵ, κ, N) in Eq. (19) to each independently vary by the experimental uncertainties. Figure 14 shows the results for 10^6 trials. The 1-σ (68%

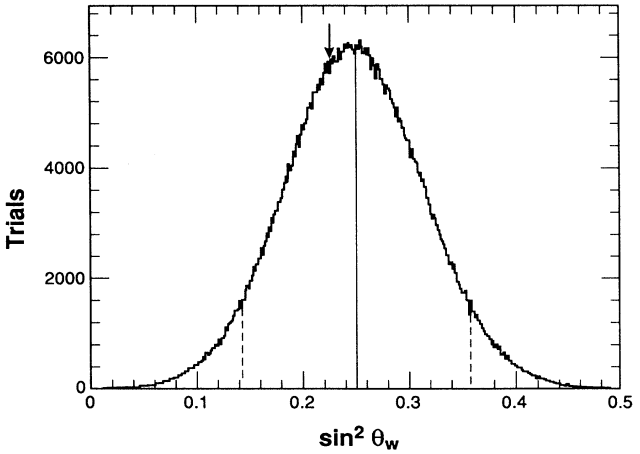

FIG. 14. $\sin^2\theta_W$ for an ensemble of Monte Carlo experiments. The results from this measurement (solid vertical line) and from collider experiments (arrow) are shown. The 90% confidence interval is delimited by dashed lines.

confidence) interval is given by $\sin^2\theta_W = 0.249 \pm 0.063$, where the error combines the statistical and systematic uncertainties.

D. Neutrino flavor-changing neutral currents

If the neutrino emerging from the neutral current is a different flavor than the (electron-flavor) neutrino emerging from the charged current, the two amplitudes will not have a coherent interference. This provides a mechanism for detecting the flavor structure of the neutral current, and, in particular, for searching for neutrino FCNC's. As suggested by Okun [30], this concept can be simply formulated in terms of diagonal (f_{ee}) and off-diagonal ($f_{e\mu}$ and $f_{e\tau}$) couplings for neutral-current mixing of neutrino flavors; for agreement with experiment the couplings are normalized to $1 = f_{ee}^2 + f_{e\mu}^2 + f_{e\tau}^2$. From the normalization requirement, the existence of flavor-changing couplings $f_{e\mu}$ or $f_{e\tau}$ would cause the diagonal coupling f_{ee} to be less than one.

The value of $\sin^2\theta_W$ measured in this experiment ($\nu_e e^-$ elastic scattering) can be compared to $\sin^2\bar{\theta}_W$ from non-neutrino experiments (W-boson and Z-boson mass measurements) to place limits on the size of $1 - f_{ee}$ according to

$$1 - f_{ee} = (\sin^2\bar{\theta}_W - \sin^2\theta_W)[1 + \tfrac{4}{3}(\sin^2\bar{\theta}_W + \sin^2\theta_W)] \times (1 - 2\sin^2\theta_W)^{-1} \ . \quad (20)$$

A recent analysis [31] of these data has found $f_{ee} > 0.65$ (90% C.L.). This minimum value for the diagonal lepton coupling can be restated as a limit for an off-diagonal, flavor-changing coupling, as $1 - f_{ee} < 0.35$ at 90% C.L., or as a limit on the total strength of flavor-changing transitions of $f_{e\mu}^2 + f_{e\tau}^2 < 0.58$ (90% C.L.).

E. Limits on neutrino electromagnetic properties

There is good agreement between the measured value of the weak mixing parameter $\sin^2\theta_W = 0.249 \pm 0.063$ and the value predicted from the high-energy collider results [32] for $\sin^2\bar{\theta}_W = 1 - M_W^2/M_Z^2$, $\sin^2\bar{\theta}_W = 0.227$. This agreement can be used to place immediate limits on the size of the radiative correction ($\delta = \sin^2\theta_W - \sin^2\bar{\theta}_W$) to the electron vector coupling constant $g_V = \bar{g}_V + 2\delta$, with $g_V = -\frac{1}{2} + 2\sin^2\theta_W$ and $\bar{g}_V = -\frac{1}{2} + 2\sin^2\bar{\theta}_W$. The 90% confidence interval for g_V (based on $0.143 < \sin^2\theta_W < 0.357$) is measured to be $-0.216 < g_V < 0.214$. The radiative correction δ to the vector coupling $\bar{g}_V = -0.046$ is therefore in the range

$$-0.170 < 2\delta < 0.260 \quad (21)$$

at the 90% confidence level. Using the relationship $\delta = (\sqrt{2}\pi\alpha/3G_F)\langle r^2\rangle$ we can convert the above confidence interval into limits on the electron-neutrino charge radius:

$$-3.56 \times 10^{-32} < \langle r^2\rangle < 5.44 \times 10^{-32} \text{ cm}^2 \ , \quad (22)$$

or more simply $|r| < 2.3 \times 10^{-16}$ cm. These bounds are consistent with results reported earlier by this experiment [18]. Although these limits represent the first laboratory limits on the size of the internal structure of the electron neutrino, the experimental precision on g_V must be improved by more than an order of magnitude to be sensitive to the expected SM radiative corrections and so to provide a definitive test of the SM radiative correction scheme.

The neutrino magnetic moment is another fundamental electromagnetic property that can be tested in neutrino-electron scattering. If the magnetic moment were sufficiently large, the event rate for neutrino electron scattering could also have a contribution from the incoherent addition of magnetic-moment scattering. We test the magnetic moment of both electron- and muon-neutrino neutrinos by comparing the observed elastic scattering event rate with the expectations of the SM with $\sin^2\theta_W = 0.227$. Because the signature for elastic scattering is determined by kinematics, the shape of the angular distribution is approximately the same for both magnetic and weak scattering; therefore, a fit to the experimental angular distribution is used to determine the elastic scattering signal. In the fit, the neutrino-induced ν_e ^{12}C background rate was normalized to the value measured separately during the course of this experiment [27]. This procedure results in a measurement of 274±37 elastic scattering events, a fixed value of 626 ν_e ^{12}C events, 136 other neutrino-nuclear interactions, and 442±75 remaining neutron-induced background events. Although magnetically scattered electrons would have a softer recoil spectrum than weakly scattered electrons, both are kinematically focused to forward recoil angles. It is not possible to distinguish in this experiment conventional weak scattering from magnetic scattering, so the observed event rate can be treated as the sum of SM elastic scattering and a possible contribution from magnetic-dipole scattering. The SM rate for the angular distribution is $R^{\text{SM}} = 285 \pm 26$ events. Comparing the SM rate to the 274 ± 35 measured events, at 90% confidence, there are fewer than 68 events due to magnetic scattering. Our sensitivity to magnetic scattering is obtained from folding Eq. (10) with the appropriate energy distributions for the neutrino flux and the detector efficiency. Because these distributions have slopes opposite to that of the cross section expression [Eq. (10)], there is little dependence upon the value of the experimental threshold T; our actual effective threshold was about 10 MeV. Using Eq. (10) and accounting for the neutrino flux and the experimental detection efficiencies, the observed event rate can be interpreted as limits on the magnetic moment of the muon and electron neutrinos [14],

$$\mu_{\nu_e}^2 + 2.1\mu_{\nu_\mu}^2 < 1.16 \times 10^{-18}\mu_{\text{Bohr}}^2, \quad (23)$$

and therefore

$$\mu_{\nu_e} < 10.8 \times 10^{-10}\mu_{\text{Bohr}} \ \ (\mu_{\nu_\mu} = 0), \quad (24)$$

$$\mu_{\nu_\mu} < 7.4 \times 10^{-10}\mu_{\text{Bohr}} \ \ (\mu_{\nu_e} = 0), \quad (25)$$

$$\mu_\nu < 6.1 \times 10^{-10}\mu_{\text{Bohr}} \ \ (\mu_\nu = \mu_{\nu_e} = \mu_{\nu_\mu}) \ . \quad (26)$$

The limit for electron neutrinos confirms bounds obtained with reactor antineutrinos [15]. The limit for muon neutrinos is the most stringent bound obtained by direct laboratory experiment. This is the only ex-

TABLE VII. Experimental quantities used to determine experimental event rates. $\epsilon_{A,B,C}$ refer to detection efficiencies for recoil electrons with $d\sigma/dy \propto 1$, $(1-y)$ and $(1-y)^2$, respectively.

Neutrino type	Detection efficiency ϵ_A	ϵ_B	ϵ_C	$\langle E_\nu \rangle$ (MeV)	$\kappa = T\phi\sigma_0$ (Events)
ν_e	0.168	0.088	0.037	31.7	618
ν_μ	0.121	0.064	0.015	29.8	581
$\overline{\nu}_\mu$	0.221	0.129	0.061	37.0	721

periment to obtain combined bounds for both neutrino types.

F. New bosons

Finally, we can place limits on the exchange of scalar, vector, or tensor bosons, which are not included in the SM. Limits on the mass of an additional Z' neutral-vector boson, based on our published interference measurement [2], have been given already by Grifols [33]. For other bosons, the observed rate for $\nu_e e^-$ elastic scattering, 236 ± 35, is to be compared to the SM prediction[3] ($\sin^2\theta_W$=0.227) of 223 ± 20. Therefore, at 90% confidence level, anomalous (beyond the SM) interactions contribute fewer than 74 events; these limits also imply that new interactions that interfere destructively with the SM amplitudes remove fewer than 58 events. Similar considerations yield 90% confidence level limits of fewer than 68 (58) events for additions (reductions) to the $\nu_e e^-$ interference term, and fewer than 78 events for additions to the total νe^- scattering rate. For example, the strength of the contribution of any new interaction to the $\nu_e e^-$ cross section, $\Delta\sigma$, after accounting for the experimental detection efficiency $\epsilon_{\rm new}$ for the proposed cross sections, must be small enough to fall within the bound

$$\Delta\sigma < \frac{\epsilon_{\rm SM}}{\epsilon_{\rm new}} \frac{74}{223} \sigma_{\rm SM} , \tag{27}$$

with $\epsilon_{\rm SM} = 0.164$ and $\sigma_{\rm SM} = 2.20\ \sigma_0$ for $\sin^2\theta_W = 0.23$.

If terms proportional to m_e/E_ν are ignored, then the differential cross section for *any* interaction composed of the sum of S, P, T, V, A components (including the SM) can be expressed as $d\sigma/dy \propto A + B(1-y) + C(1-y)^2$ and the total cross section is simply $\sigma = (A + B/2 + C/3)\sigma_0$. For the SM with $\sin^2\theta_W = 0.23$, the coefficients are given by $A_{\rm SM} = 2.14$, $B_{\rm SM} = 0$, and $C_{\rm SM} = 0.17$. Therefore, the expected event rate for any proposed interaction can be obtained uniquely in terms of its couplings (A, B, C) and the appropriate detection efficiencies. The experimental quantities are summarized in Table VII.

For example, consider the exchange of a charged-scalar (Higgs) boson, χ^+, as shown in the Feynman diagram of Fig. 15. The $\nu_e e^-$ scattering cross section [34] for the sum of SM and χ^+ exchange contributions is

$$\frac{d\sigma}{dy} = \frac{d\sigma_{\rm SM}}{dy} - 4\sigma_0 \left[2\left(\frac{\eta M_W}{g M_\chi} \sin\theta_W\right)^2 - 4\left(\frac{\eta M_W}{g M_\chi}\right)^4 \right] \times (1-y)^2 . \tag{28}$$

The $Z - \chi$ interference term and the incoherent term both appear with a factor of $(1-y)^2$ in the differential cross section. This energy dependence severely reduces the experimental sensitivity, yielding the limit on the new terms of

$$\epsilon_C \frac{8}{3}(2\chi^4 - \sin^2\theta_W\, \chi^2) < 0.120 , \tag{29}$$

where $\chi = (\eta M_W)/(g M_\chi)$, and the detection efficiency for the $(1-y)^2$ term is $\epsilon_C = 0.037$. This expression is solved as $M_\chi > 1.09(\eta/g) M_W$. For a Higgs-lepton coupling equal to the SM SU(2) gauge coupling, we find a limit of $M_{\chi^+} > 87$ GeV.

Under the assumption that the new bosons couple with equal strength to electron and muon neutrinos, a neutral boson interaction can be better studied by utilizing the scattering of all three neutrino types: ν_e, ν_μ, and $\overline{\nu}_\mu$. We can use the total observed elastic scattering rate from Sec. IV B, $R(\nu e^-) = 295 \pm 35$ events, to increase sensitivity. Any new interaction would introduce events at a rate

$$R = \Sigma_{i=\nu_e,\nu_\mu,\overline{\nu}_\mu} (\epsilon_A^i A_i + \tfrac{1}{2}\epsilon_B^i B_i + \tfrac{1}{3}\epsilon_C^i C_i)\kappa_i < 78 \text{ events} , \tag{30}$$

where the values of $\epsilon_{A,B,C}^i$ and κ_i are obtained from Table VII, and the coefficients A_i, B_i, and C_i depend upon the tensorial character of the interaction as discussed below.

The limits on the rate R are solved to obtain limits on the coupling strengths (A, B, C) of the new interaction. The limits on exotic couplings $G_{\rm new}$ can be interpreted in terms of a ratio of boson-mass and in-

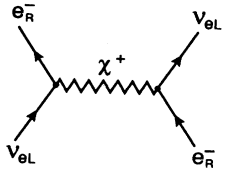

FIG. 15. Feynman diagram for charged Higgs boson χ^+ exchange in $\nu_e e^- \to \nu_e e^-$ scattering. Note that this diagram will interfere with the SM Z^0-exchange amplitude.

[3]The SM contributions are 223 $\nu_e e^-$, 21 $\nu_\mu e^-$, and 38 $\overline{\nu}_\mu e^-$ events.

trinsic gauge couplings of the new interaction according to $G_{\rm new} = \frac{1}{2}(\eta/g)(M_Z/M^*)$ for a neutral boson or $G_{\rm new} = 2(\eta/g)(M_W/M^*)$ for a charged boson. Here, g is the SM gauge coupling to SU(2) isospin, and η, M^* are the gauge coupling and mass of the hypothetical boson. In the following paragraphs, limits are explicitly calculated for new neutral bosons with spin 0 or 2, and for any new (neutral or charged) boson with purely left-handed $(V-A)$ couplings.

Any purely NC interaction with (S, P, or T) couplings would imply the existence of a right-handed neutrino, since the lepton helicity is altered at the exchange vertex. As the outgoing neutrino would be right handed, the (S, P, T) components of the NC would not interfere coherently with $W^{\pm}$ or Z^0 exchange; the new interaction could only add incoherently to the SM event rate. It can be shown [4] that S, P, T couplings would introduce additional terms into the cross section given by

$$A = \tfrac{1}{16}\{(S+P)^2 + [(S-P) - 4T]^2\}, \quad (31)$$

$$B = 2\{T^2 - \tfrac{1}{16}[(S+P)^2 + (S-P)^2]\}, \quad (32)$$

$$C = \tfrac{1}{16}\{(S+P)^2 + [(S-P) + 4T]^2\}, \quad (33)$$

where, for example, $T = \frac{1}{2}(\eta_T M_Z/gM_T)^2$ relates the cross section to the mass and gauge coupling of the neutral tensor boson. For antineutrino scattering, the terms A and C would be interchanged.

We extract general limits on the mass/couplings ratios for scalar and tensor interactions. For the case of a purely spin-2 T interaction ($S = P = 0$), we find that $R = T^2(543.2) < 78$, or $T = \frac{1}{2}(\eta_T M_Z)/(gM_T) < 0.379$. If the tensor boson couples with same strength as the weak neutral current ($\eta_T = g$), this limit would imply that the neutral tensor boson must be heavier than $M_T > 1.15M_Z \approx 105$ GeV. For a spin 0 boson (pure scalar S or pseudoscalar P), the B term has the opposite sign, so the limits become $(P^2/8$ or $S^2/8) < 0.448$. Assuming just one boson with gauge couplings equal to the SM couplings to the Z, the (pseudo)scalar boson mass must be greater than $M_{P,S} > 0.51M_Z \approx 47$ GeV.

Other types of hypothetical interactions are more complicated to evaluate because of possible interference terms with the SM amplitudes. For example, consider a purely left-handed vector boson that couples to electrons and neutrinos. From the symmetry between the charged- and neutral-current couplings C_L and g_L in Eq. (7), we see that the new terms enter the cross section in the same way for either a charged or neutral left-handed boson. However, the charged- or neutral-boson terms enter with different couplings and would exhibit a phase ϕ relative to the $W^{\pm}$ or Z^0. We will calculate limits for purely destructive ($\cos\phi = -1$) or purely constructive ($\cos\phi = +1$) interference. If we use $X = 2(\eta_x M_W/gM_x)^2$ to define the coupling for a charged boson, then we can solve for X as

$$\epsilon_A^{\nu_e}\kappa_{\nu_e}[X^2 \pm (2 + 4\sin^2\theta_W)X] < 74\,, \quad (34)$$

where the first term is the contribution from the new boson, and the second term is the interference between the new boson and the SM bosons. For a constructive interference (+), we find that $X < 0.227$, which implies, for gauge couplings equal to the $W^{\pm}$, that the left-handed vector boson has $M_x > 2.97M_W \approx 239$ GeV. A negative interference (removing fewer than 58 events) results in a limit of $X < 0.183$, or $M_x > 3.33M_W \approx 268$ GeV for the usual assumptions. Because of the different couplings, the limits for a neutral left-handed boson are weaker: after summing over the scattering for all three neutrinos, ν_e, ν_μ, and $\overline{\nu}_\mu$, we find that $M_x > 119$ GeV for constructive interference and that $M_x > 130$ GeV for destructive interference.

TABLE VIII. Limits on new gauge boson masses for coupling strengths equal to the appropriate charged or neutral SM coupling.

Coupling	Charge	Mass limit (GeV)
T	Neutral	105
S, P	Neutral	47
Higgs boson (S)	Charged	87
Left handed (V, A)	Neutral	119
Left handed (V, A)	Charged	240

These results are collected in Table VIII. In general, the limits are similar to those obtained from collider measurements but are subject to fewer assumptions.

VI. CONCLUSIONS

We have measured $\nu_e e^-$ elastic scattering to sufficient precision to unambiguously demonstrate the destructive nature of the interference between the charged and neutral current amplitudes. The absolute cross section and the interference strength were measured to 17.5% accuracy; they are in excellent agreement with SM predictions including $W^{\pm}$ and Z^0 interference effects. The good agreement of the observed event rate with the predictions of the SM is used to place new limits upon the electromagnetic properties of electron and muon neutrinos and upon FCNC.

The close agreement of the observed scattering rate with that predicted by the SM also allows us to place limits on the masses of new scalar, vector, or tensor bosons not in the SM. For couplings of the same strength as the SM gauge coupling to SU(2) isospin, we find that a neutral tensor boson must be heavier than $M_T > 105$ GeV, that a neutral (pseudo)scalar boson must be heavier than $M_{P,S} > 47$ GeV, that a charged Higgs boson must be heavier than $M_{\chi^+} > 87$ GeV, and that any charged (neutral) vector boson with purely left-handed couplings must be heavier than $M_x > 239$ (119) GeV. In general, limits obtained here on the mass of hypothetical bosons are similar to limits obtained by direct searches for such bosons in collider experiments. However, limits from neutrino-electron scattering may be important for ruling out particular extensions of the SM, which involve bosons that couple mainly, or only, to leptons. An interesting type of reaction, that only this experiment can address, is a weak interaction that exclusively couples fermions within the same weak isodoublet.

ACKNOWLEDGMENTS

The successful completion of this experiment depended crucially upon the dedicated efforts of many people. N. Briscoe, C. G. Dalton, R. S. DeLay, G. J. Krausse, A. J. Sena, J. Sims, and T. N. Thompson provided superior technical support while designing, building, operating, maintaining, and upgrading the detector. C. Lindsay handled the data replay and K. Roemheld made significant contributions to the analysis codes. V. Bharadwaj, G. Brooks, S. Chesney, J. Courtney, M. Duong-van, H. Juds, and M. Rushton helped in the initial construction of this experiment. W. Johnson and H. Yao contributed to portions of the data analysis. We are grateful to L. Agnew, F. Reines, and L. Rosen for their support and encouragement and to P. Herczeg, J. N. Ng, S. P. Rosen, and R. Shrock for useful discussions and comments. We thank M. Roberta and J. Harris for enlightening conversations, and S. A. Stolberg for essential assistance at several critical junctures. This work was supported in part by the U.S. National Science Foundation, PHY85-01559 and the U.S. Department of Energy, Nuclear Physics Division and High Energy Physics Division, under Contract Nos. DE-AC05-76ERO-2504, W-31-109-ENG-38, and W-7405-ENG-36.

[1] R.C. Allen *et al.*, Phys. Rev. Lett. **55**, 2401 (1985).
[2] R.C. Allen *et al.*, Phys. Rev. Lett. **64**, 1330 (1990).
[3] G. 't Hooft, Phys. Lett. **37B**, 195 (1971).
[4] B. Kayser, E. Fischbach, S.P. Rosen, and H. Spivack, Phys. Rev. D **20**, 87 (1979).
[5] U. Amaldi *et al.*, Phys. Rev. D **36**, 1385 (1987).
[6] F. Reines, H.S. Gurr, and H. Sobel, Phys. Rev. Lett. **37**, 315 (1977).
[7] OPAL Collaboration, M.Z. Akrawy *et al.*, Z. Phys. C **50**, 373 (1991).
[8] CHARM II Collaboration, D. Geiregat *et al.*, Phys. Lett. B **245**, 271 (1990).
[9] S.R. Mishra *et al.*, Phys. Rev. Lett. **66**, 3117 (1991).
[10] G. Bardin *et al.*, Phys. Lett. **137B**, 135 (1984).
[11] J. Dorenbosch *et al.*, Z. Phys. C **41**, 567 (1989).
[12] L.A. Ahrens *et al.*, Phys. Rev. D **41**, 3301 (1990).
[13] L.M. Sehgal, Phys. Lett. **55B**, 205 (1975).
[14] D.A. Krakauer *et al.*, Phys. Lett. B **252**, 177 (1990).
[15] A.V. Kuyldjiev, Nucl. Phys. **B243**, 387 (1984). Recent reanalysis of Ref. [6] has resulted in a less restrictive bound on the $\overline{\nu}_e$ magnetic moment; see P. Vogel and J. Engel, Phys. Rev. D **39**, 3378 (1989).
[16] Robert E. Shrock, Nucl. Phys. **B206**, 359 (1982); B.W. Lee and R.E. Shrock, Phys. Rev. D **16**, 1444 (1977).
[17] G. DeGrassi, A. Sirlin, and W.J. Marciano, Phys. Rev. D **39**, 287 (1989).
[18] R.C. Allen *et al.*, Phys. Rev. D **43**, R1 (1991).
[19] R.C. Allen *et al.*, Nucl. Instrum. Methods A **269**, 177 (1988).
[20] R.L. Burman, M.E. Potter, and E.S. Smith, Nucl. Instrum. Methods A **291**, 621 (1990).
[21] R.C. Allen, H.H. Chen, M.E. Potter, R.L. Burman, J.B. Donahue, D.A. Krakauer, R.L. Talaga, E.S. Smith, and A.C. Dodd, Nucl. Instrum. Methods A **284**, 347 (1989).
[22] K.C. Wang and H.H. Chen, IEEE Trans. Nucl. Sci. **NS-28**, 405 (1981); C. Dalton and G. Krausse, Nucl. Instrum. Methods A **158**, 289 (1979); G.J. Krausse, C.G. Dalton, and J. Sargeant, presented at the 14th Pulse Power Symposium, 1980, Los Alamos National Laboratory Report No. LA-UR-80-1361 (unpublished).
[23] R.C. Allen, G.A. Brooks, and H.H. Chen, IEEE Trans. Nucl. Sci. **NS-28**, 487 (1981).
[24] W.R. Nelson, H. Hirayama, and D.W.O. Rogers, The EGS4 Code System, Technical Report, Stanford Linear Accelerator Center, Report No. 265, 1985 (unpublished).
[25] T.W. Donnelly, Phys. Lett. **43B**, 93 (1973); and (private communication).
[26] R.C. Allen *et al.*, The Large Čerenkov Detector Project, Los Alamos National Laboratory Report No. LA-UR-11300-P, 1988 (unpublished).
[27] R.C. Allen *et al.*, Phys. Rev. Lett. **64**, 1871 (1990); D.A. Krakauer *et al.*, Phys. Rev. C **45**, 2450 (1992).
[28] M.E. Potter, Ph.D. thesis, University of California, Irvine, 1987; Los Alamos National Laboratory Report No. LA-UR-11182-T, 1988 (unpublished).
[29] B. Schumm, Ph.D. thesis, University of Chicago, 1988.
[30] L.B. Okun, Yad. Fiz. **41**, 1272 (1985) [Sov. J. Nucl. Phys. **41**, 812 (1985)].
[31] D.A. Krakauer *et al.*, Phys. Rev. D **45**, 975 (1992).
[32] Based upon a recent world average, as summarized by the CDF Collaboration, F. Abe *et al.*, Phys. Rev. D **43**, 2070 (1991).
[33] J.A. Grifols, Mod. Phys. Lett. A **31**, 2657 (1990).
[34] John N. Ng, Phys. Rev. D **31**, 464 (1985).